nature physics

Article

https://doi.org/10.1038/s41567-024-02626-6

Energy partitioning in the cell cortex

Received: 27 October 2023

Accepted: 1 August 2024

Published online: 12 September 2024

Check for updates

Sheng Chen [1,2], Daniel S. Seara [2,3,4], Ani Michaud [5,6], Songeun Kim [5,6], William M. Bement [5,6,7,8] ✉ & Michael P. Murrell [1,2,3,8] ✉

Living systems are driven far from thermodynamic equilibrium through the continuous consumption of ambient energy. In the cell cortex, this energy is invested in the formation of diverse patterns in chemical and mechanical activities, whose spatial and temporal dynamics determine the cell phenotypes and behaviours. How cells partition internal energy between these activities is unknown. Here we measured the entropy production rate of both chemical and mechanical subsystems of the cell cortex across a variety of patterns as the system is driven further from equilibrium. We do this by manipulating the Rho GTPase pathway, which controls the cortical actin filaments and myosin-II. At lower levels of GTPase-activating protein expression, which produce pulses or choppy Rho and actin filament waves, energy is proportionally partitioned between the two subsystems and is subject to the constraint of Onsager reciprocity. Within the range of reciprocity, the entropy production rate is maximized in choppy waves. As the cortex is driven into labyrinthine or spiral travelling waves, reciprocity is broken, marking an increasingly differential partitioning of energy and an uncoupling of chemical and mechanical activities. We further demonstrate that energy partitioning and reciprocity are determined by the competing timescales between chemical reaction and mechanical relaxation.

Living cells harness energy from the environment to drive out-of-equilibrium processes that promote and sustain life[1–6]. As non-equilibrium systems, cells extend classic thermodynamic principles, such as the second law (entropy production, $\Delta S \geq 0$)[7,8]. Further, the complexity of subcellular processes poses a serious challenge in determining the rules that govern cellular metabolic energy expenditure in vivo[1,2]. For example, although recent studies measure cellular/organismal energy metabolism via calorimetry[9–12], adenosine triphosphate (ATP) fluorescence[13] and metabolic or respiratory fluxes[14–17], these techniques measure the total energy, and cannot isolate the energy dissipated by concurrent internal processes that ultimately share the same source of energy. Consequently, how metabolic energy is used by and partitioned between non-equilibrium subsystems and how this relates to biological outcomes remain enigmatic.

The eukaryotic cell cortex is a key driver of cell migration[18–22], morphogenesis[23–28] and cell division[29–32], providing an ideal system to study energetic partitioning strategies at the intracellular level in vivo. The cell cortex comprises the plasma membrane and the underlying cytoskeleton, and the cell cortex itself can be considered to be composed of two subsystems. The first is a mechanical subsystem based on actin filaments (F-actin), the motor protein myosin-II and other actin-binding proteins that perform mechanical work via the consumption of ATP[33,34]. The second is a chemical signalling subsystem based on the G-protein Rho, which regulates F-actin and myosin-II by cycling between an active guanosine triphosphate (GTP)-bound form and an inactive guanosine-diphosphate-bound form and thus directs cortical patterns based on the consumption of GTP. The interaction of these two systems makes the cell cortex a mechanochemical, dissipative and

[1]Department of Biomedical Engineering, Yale University, New Haven, CT, USA. [2]Systems Biology Institute, Yale University, West Haven, CT, USA. [3]Department of Physics, Yale University, New Haven, CT, USA. [4]James Franck Institute, University of Chicago, Chicago, IL, USA. [5]Cellular and Molecular Biology Graduate Program, University of Wisconsin–Madison, Madison, WI, USA. [6]Center for Quantitative Cell Imaging, University of Wisconsin–Madison, Madison, WI, USA. [7]Department of Integrative Biology, University of Wisconsin–Madison, Madison, WI, USA. [8]These authors contributed equally: William M. Bement, Michael P. Murrell. ✉e-mail: wmbement@wisc.edu; michael.murrell@yale.edu

excitable medium that can exhibit a variety of self-organized, periodic signalling, and mechanical patterns[16,28,31,35–38], each associated with different phenotypic outcomes. For example, Rho and actomyosin pulses drive polarization in *C. elegans*[23] and morphogenesis in *Drosophila* embryos[26], and travelling waves of Rho and actomyosin drive cytokinesis in starfish and *Xenopus* embryos[31]. Here we have exploited the periodic, quasi-two-dimensional nature of cortical pulses and travelling waves to study how energy is partitioned between the chemical and mechanical subsystems of the cell cortex under conditions where patterns are induced and systematically varied.

Increased RGA-3/4 expression drives the cell cortex from quiescence through diverse excitable patterns

To systematically investigate how the cortex partitions energy between the chemical and mechanical subsystems, we expressed two cytokinetic regulators in immature *Xenopus* oocytes: Ect2, a protein that promotes the exchange of guanosine diphosphate for GTP by Rho; and RGA-3/4 (also known as ArhGAP11A or MP-GAP), a protein that promotes the hydrolysis of GTP by Rho. The assembly of F-actin is stimulated by Rho, whereas Rho itself is inactivated by RGA-3/4, which associates with F-actin. F-actin collaborates with myosin-II to transmit contractile force, triggering cortical deformation. Cortical deformation, in turn, impacts the chemical dynamics through advection. (Fig. 1a,b shows the schematic). The combined expression of Ect2 and RGA-3/4 converts the normally quiescent oocyte cortex into an excitable medium in which waves of Rho activity and 'chasing waves' of F-actin, RGA-3/4 and myosin-II develop[39]. Although these waves mimic those observed in the cytokinetic furrow of dividing *Xenopus* and starfish embryos[31], they are visible for many minutes (in contrast to furrow waves that rapidly ingress out of reach of the microscopy objective), rendering them amenable to quantitative analysis. Further, when the concentration of RGA-3/4 is varied against a background of constant Ect2 expression to modulate the consumption of GTP by Rho, a variety of periodic patterns are produced, ranging from pulses to short-wavefront choppy travelling waves, labyrinthine travelling waves and spiral waves (Fig. 1c, Supplementary Video 1 and ref. 39). The expected outcome of the increased RGA-3/4 expression is not only an increase in the amount of energy consumed by the chemical subsystem of the cortex (via increased GTP hydrolysis by Rho) but also increased energy consumption by the mechanical subsystem. That is, although actin assembly and myosin-II consume ATP, actin assembly and myosin-II activation are gated by active Rho via formins and Rho-dependent kinase, respectively. Further, because RGA-3/4 expression increases the cortical energy consumption, it is also expected to drive the cortex further from equilibrium, as will be established formally in the section below.

The periodic cortical patterns were quantified by the measurement of three signals, which relate to the chemical and mechanical aspects of the periodic patterns: Rho (R, chemical) and F-actin (F, chemical/mechanical) concentration oscillations were measured via fluorescence intensity (Supplementary Note I). As shown in Supplementary Fig. 4, both can be formulated as a noisy periodic oscillation, with the deterministic part expressed by a periodic sinusoidal function, plus a noise part following the Gaussian distribution. The mechanical signal was quantified via local cell cortex deformation rate ($\mathbf{v}_c$, mechanical) and strain rates (dilation rate, $\dot{\varepsilon}_d$; shear rate, $\dot{\varepsilon}_s$; mechanical), based on the contraction-induced displacement of cortical pigment granules, which was previously shown to report myosin-powered bulk flow (Supplementary Note II, Supplementary Fig. 3 and Supplementary Video 2)[40]. As previously described[39], Rho wave amplitude initially increases sharply with increasing RGA-3/4 concentration ([RGA-3/4]), but then reaches a plateau (Supplementary Fig. 2). F-actin wave amplitude follows a similar pattern (Supplementary Fig. 2). Curiously, however, after initially rising with increasing [RGA-3/4], the dilation rate—rather than plateauing—underwent a progressive decline back to the level obtained in the absence of RGA-3/4 (Fig. 1d).

To independently assess the consequences of the experimental elevation of energy consumption by chemical and mechanical subsystems, a computational model that combines signalling and mechanics via reaction–diffusion–advection equations with a coupled viscoelastic cortex material was developed (Supplementary Note III). In this model, the increasing [RGA-3/4] was represented by increasing k_{RGA}, which defines the hydrolysis rate of Rho-GTP promoted by the expression of RGA-3/4. This model faithfully captures the RGA-3/4-induced changes in two-dimensional cortical patterns seen in experiments (Supplementary Fig. 1 and Supplementary Video 3).

RGA-3/4 expression determines energy partitioning in the cell cortex

These visible biochemical oscillatory waves are the consequence of multiple molecular-level irreversible cycles that consume energy. We measured the entropy production rates ((EPR) denoted as $\dot{S}$) associated with progressively elevated [RGA-3/4]. EPR reflects the irreversibility of system dynamics[41,42] and is related to the dissipated energy. At steady state, the input energy is balanced by the energy output. The EPR represents a measure of the minimum energy required to sustain the observed process. Consequently, it offers a lower-bound quantification to the input of energy, or the energetic cost, to sustain the periodic cortical patterns. The total EPR ($\dot{S}_{total}$) can be split into two non-negative groups[43,44]: EPRs produced by each of the signals individually (Rho, F-actin and granules' deformation, giving $\dot{S}_R$, $\dot{S}_F$ and $\dot{S}_c$, respectively) and EPRs produced by two interacting signals ($\dot{S}_{RF}$, $\dot{S}_{Fd}$ and $\dot{S}_{Rd}$). We take $\dot{S}_{total} = \left(\dot{S}_R + \dot{S}_F + \dot{S}_c\right) + \left(\dot{S}_{RF} + \dot{S}_{Fd} + \dot{S}_{Rd}\right)$. By investigating the EPR generated by different chemical and mechanical dynamics, we are able to understand the energy partitioning among different subsystems (that is, E_{sub}/E_{total}) inside the cell cortex with the assumption that $E_{sub}/E_{total} \approx \dot{S}_{sub}/\dot{S}_{total}$.

First, we quantified $\dot{S}$ of each individual signal in the cell cortex by independently measuring the temporal autocorrelation for R, F and $\mathbf{v}_c$. Autocorrelation functions of noisy oscillatory dynamics are typically given by sinusoidal functions oscillating with frequency f, measuring the average rate of oscillation, with an amplitude that decays exponentially with a timescale defined by the coherence time τ, measuring the regularity of oscillations[45–47]. The energy required to run a noisy oscillator increases when the signal oscillates faster (increasing f) or more reliably (increasing τ). $\dot{S}$ was estimated as $\dot{S} = f^2\tau$ (Supplementary Note II (wave coherence method)). Here f (Fig. 2a) and τ (Fig. 2b) were extracted from the corresponding autocorrelation function (Supplementary Note II and Supplementary Fig. 5). We measured the $\dot{S}$ value produced by chemical signalling from the Rho and F-actin dynamics ($\dot{S}_R$ and $\dot{S}_F$), as well as by mechanical activities from the cortex deformation rate $\mathbf{v}_c$, dilation rate $\dot{\varepsilon}_d$ and shear rate $\dot{\varepsilon}_s$ ($\dot{S}_c$, $\dot{S}_{dil}$ and $\dot{S}_{shr}$, respectively). We find that the positive monotonicity of both f and τ at low [RGA-3/4] makes $\dot{S}$ for all the signals grow with [RGA-3/4]. At high [RGA-3/4], the positive monotonicity of f and the negative monotonicity of τ compensate, making $\dot{S}_R$ and $\dot{S}_F$ plateau, whereas $\dot{S}_c$, $\dot{S}_{dil}$ and $\dot{S}_{shr}$ peak and decrease (Fig. 2c and Supplementary Fig. 7). Overall, $\dot{S}$ measured in simulation through autocorrelations and two other alternative methods align with the observed trends in experimental data (Fig. 2f, Supplementary Fig. 9 and Supplementary Note II).

Comparing the quantifications (Fig. 2) to the patterns (Fig. 1) shows that as [RGA-3/4] increases, $\dot{S}$ for the chemical subsystems grows as pulses give way to choppy travelling waves and then plateaus as choppy waves give way to labyrinthine and spiral travelling waves. In contrast, although $\dot{S}$ for the mechanical subsystem also initially increases in response to increasing [RGA-3/4], it drops at higher levels, corresponding to the point where choppy waves transition to labyrinthine travelling waves. Thus, interactions between the different

https://doi.org/10.1038/s41567-024-02626-6

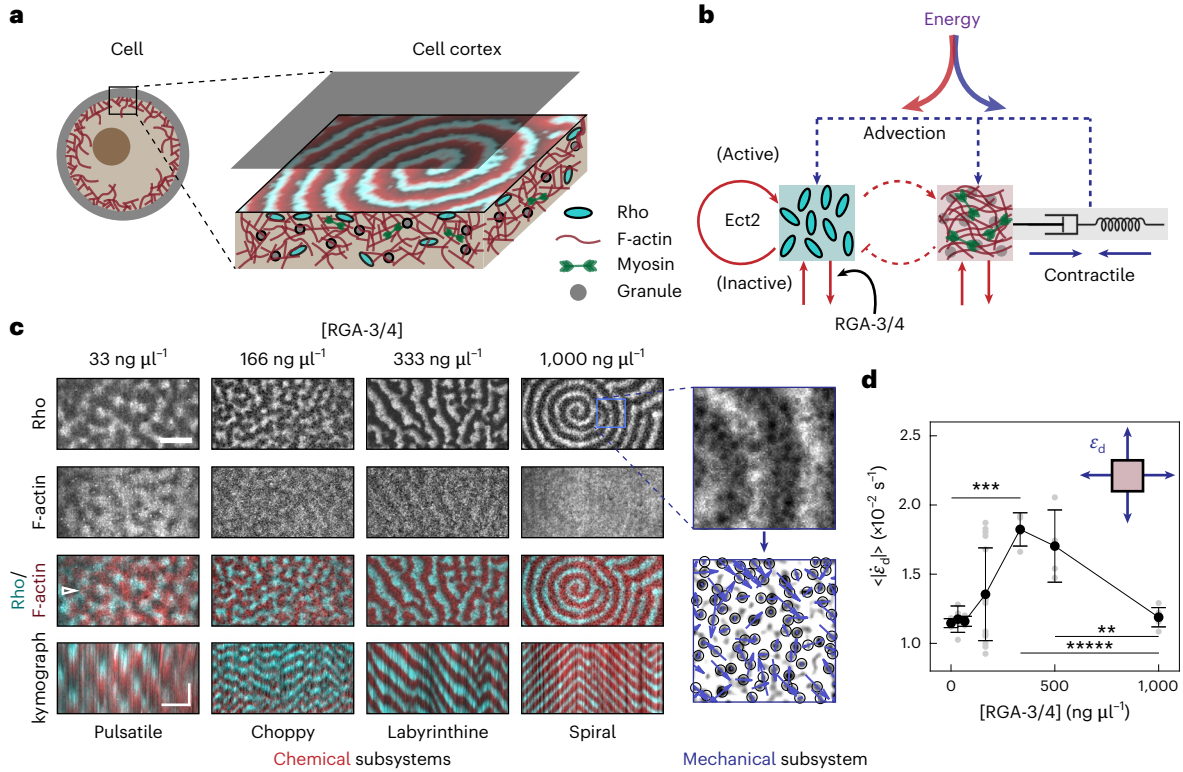

Fig. 1 | RGA-3/4 expression drives diverse mechanochemical patterns in the cell cortex. a, Schematic of the plot of the Rho/F-actin wave in the cell cortex. The spiral wave is an example from the simulation results with $k_{RGA} = 0.60\ s^{-1}$. k_{RGA} defines the hydrolysis rate of Rho-GTP promoted by the expression of RGA-3/4. **b**, Schematic of the plot of the Rho/F-actin activator–inhibitor feedback loops and the coupling with the viscoelastic cell cortex. The red lines indicate the chemical reactions, and the blue lines indicate the coupled mechanical dynamics. The dashed lines indicate the interaction between two chemical subsystems (Rho and F-actin, red dashed lines), or between the chemical and mechanical subsystems through advection (blue dashed lines). The arrow lines indicate promotion, and the T-shaped line indicates inhibition. Ect2 promotes the exchange of inactive Rho for active Rho, and RGA-3/4 promotes the consumption of active Rho. **c**, Experiment. Prototypical examples of pulsatile, choppy, labyrinthine and spiral wave phenotypes with [RGA-3/4] = 33, 166, 333 and 1,000 ng µl^{-1}, respectively. From top to bottom, the rows show [Rho], [F-actin], a merged image with [Rho] and [F-actin] (shown in cyan and red, respectively), and a kymograph of the merged image (chemical signals). The kymograph is taken along a horizontal slice indicated by the open triangular symbol at the left of the merged image. Time is increasing downwards. Scale bars, 25 µm (space); 2 min (time). Right inset: zoomed-in portions from the blue box in **c**, showing the pigment granules' positions and their instantaneous velocities (blue arrows, the mechanical signal). **d**, Absolute value of the dilation rate ($|\dot{\varepsilon}_d|$) of the cortex deformation as a function of [RGA-3/4] with [RGA-3/4] = 0 ($n = 3$), 33 ($n = 5$), 66 ($n = 5$), 166 ($n = 16$), 333 ($n = 4$), 500 ($n = 4$) and 1,000 ng µl^{-1} ($n = 6$). P values are 2.4×10^{-4}, 5.1×10^{-6} and 1.5×10^{-3} between [RGA-3/4] = 0 and 333 ng µl^{-1}, [RGA-3/4] = 333 and 1,000 ng µl^{-1}, and [RGA-3/4] = 500 and 1,000 ng µl^{-1}, respectively. Data are presented as mean ± standard deviation (s.d.). All the statistical comparisons between two distributions were done with a two-sided t-test. We use the symbols **, *** and ***** for P values of 0.01, 0.001 and 0.00001, respectively.

components of the cell cortex qualitatively and quantitatively change as the energy consumed by Rho is progressively elevated.

Decoupling of the chemical and mechanical subsystems at high RGA-3/4

The above results suggest that differential energy partitioning at high RGA-3/4 results in the decoupling of chemical and mechanical subsystems of the cell cortex. As an alternative way to test this inference, we used cross-correlation between each pair of R, F and cortex dilation rate $\dot{\varepsilon}_d$ (Supplementary Note II, Fig. 2d and Supplementary Fig. 6). The $\dot{S}$ value arising from R and F interactions, namely, $\dot{S}_{RF}$, shows a similar trend as seen in the individual chemical signals, namely, a monotonic growth that leads to a plateau (Fig. 2g). In contrast, the $\dot{S}$ value arising from both R and $\dot{\varepsilon}_d$ interactions ($\dot{S}_{Rd}$) and F and $\dot{\varepsilon}_d$ interactions ($\dot{S}_{Fd}$) prominently peak and drop (Fig. 2h,i). These trends were replicated via a third method, namely, estimating the $\dot{S}$ value from interactions based on making a diffusive approximation for the dynamics[42] (Supplementary Note II and Supplementary Fig. 8), as well as in simulations (Supplementary Fig. 9). Increased variance in EPR is observed at high levels of [RGA-3/4] due to an increase in phenotypic variability and heterogeneity of the cortical waves (Supplementary Fig. 10d). Furthermore, the phase portrait analysis performed on the model corroborates the decoupling process (Supplementary Note III). As shown in Fig. 3a, with low k_{RGA}, a limit cycle forms (which suggests periodic oscillations) only when the reaction–diffusion equation is coupled with the mechanical response. As a comparison (Fig. 3c), with high k_{RGA}, a pure reaction–diffusion system can produce spontaneous Rho/F-actin oscillations that are marginally affected by the mechanical advective transport.

Collectively, these results demonstrate that the energy input into the excitable cell cortex, controllable via [RGA-3/4], gets repartitioned to the chemical and mechanical subsystems of the cell cortex. At low [RGA-3/4], an energy input leads to an increase in the $\dot{S}$ values of Rho, F-actin and mechanical deformations. However, at high [RGA-3/4], the $\dot{S}$ values of Rho, F-actin dynamics and their interactions plateau, whereas the mechanical $\dot{S}$ decreases, indicating that the mechanical activities become decoupled from chemical signalling.

Onsager reciprocity suggests energy partitioning in a fixed proportion at modest RGA-3/4

Modestly elevating [RGA-3/4] makes mechanical $\dot{S}$ ($\dot{S}_c$, $\dot{S}_{dil}$ and $\dot{S}_{shr}$) increase linearly with chemical $\dot{S}$ ($\dot{S}_R$ and $\dot{S}_F$), suggesting that $\dot{S}_{total}$ is

https://doi.org/10.1038/s41567-024-02626-6

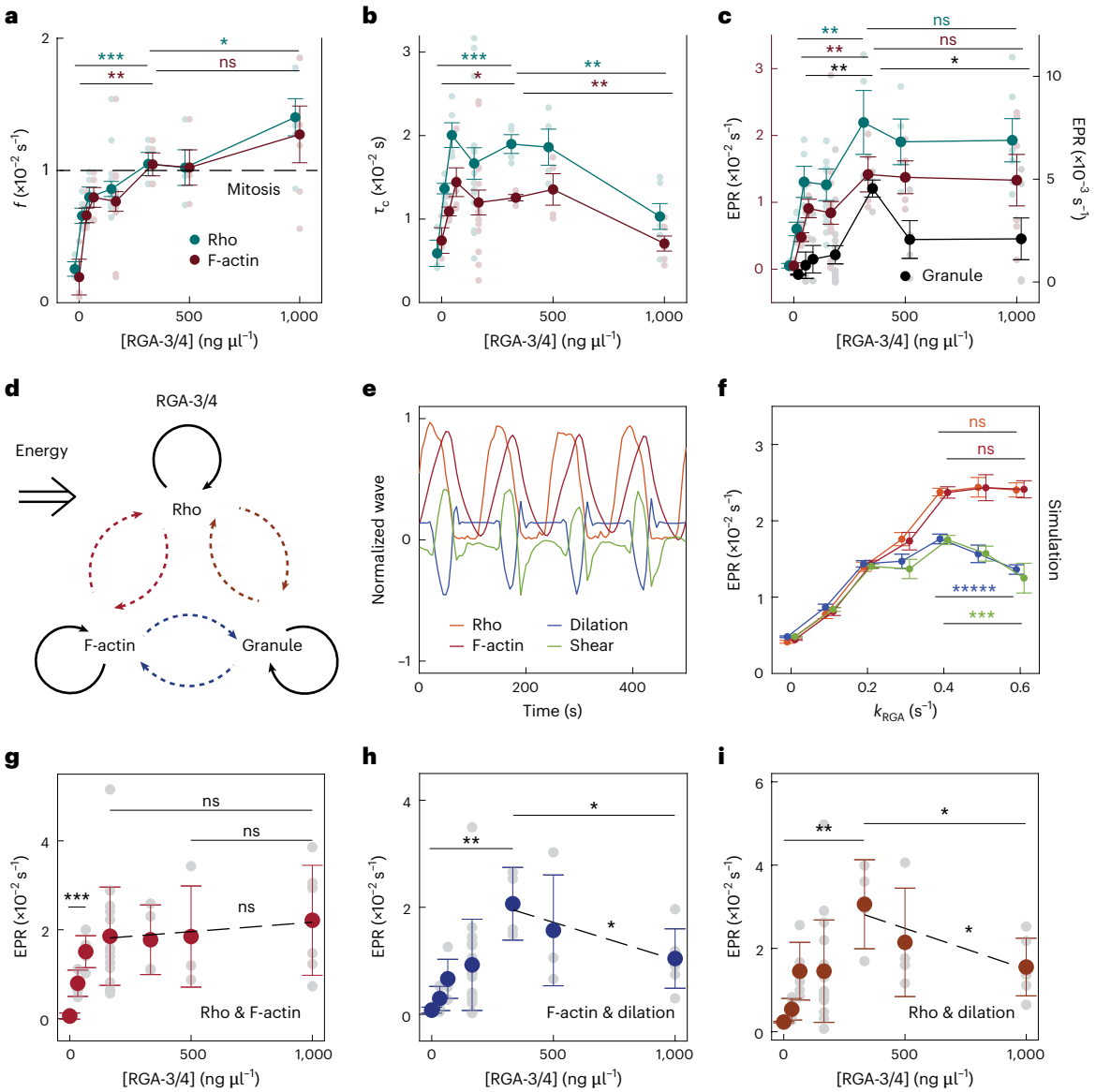

Fig. 2 | Energy partitioning between chemical and mechanical subsystems depends on RGA-3/4. a, Autocorrelation frequency (f) as a function of RGA-3/4. The dashed line indicates a frequency of 0.01 s^{-1} that is measured from the cortical waves during mitosis[57]. For Rho, $P = 9.2 \times 10^{-4}$ and 9.8×10^{-2} between [RGA-3/4] = 0 and 333 ng μl^{-1} and [RGA-3/4] = 333 and 1,000 ng μl^{-1}, respectively. For F-actin, $P = 2.5 \times 10^{-3}$ and 4.4×10^{-1} between [RGA-3/4] = 0 and 333 ng μl^{-1} and [RGA-3/4] = 333 and 1,000 ng μl^{-1}, respectively. **b**, Autocorrelation coherence time (τ) as a function of RGA-3/4. For Rho, $P = 9.3 \times 10^{-4}$ and 3.6×10^{-3} between [RGA-3/4] = 0 and 333 ng μl^{-1} and [RGA-3/4] = 333 and 1,000 ng μl^{-1}, respectively. For F-actin, $P = 1.3 \times 10^{-2}$ and 1.5×10^{-3} between [RGA-3/4] = 0 and 333 ng μl^{-1} and [RGA-3/4] = 333 and 1,000 ng μl^{-1}, respectively. **c**, EPR $\dot{S} = f^2\tau$, for Rho (cyan), F-actin (red) and granule motions (black). For Rho, $P = 8.1 \times 10^{-3}$ and 6.4×10^{-1} between [RGA-3/4] = 33 and 333 ng μl^{-1} and [RGA-3/4] = 333 and 1,000 ng μl^{-1}, respectively. For F-actin, $P = 6.1 \times 10^{-3}$ and 8.7×10^{-1} between [RGA-3/4] = 33 and 333 ng μl^{-1} and [RGA-3/4] = 333 and 1,000 ng μl^{-1}, respectively. For granule motions, $P = 2.6 \times 10^{-3}$ and 9.9×10^{-2} between [RGA-3/4] = 33 and 333 ng μl^{-1} and [RGA-3/4] = 333 and 1,000 ng μl^{-1}, respectively. **d**, Schematic of the plot of $\dot{S}$ produced by autocorrelated (black solid arrows) and cross-correlated signals (coloured dashed arrows). **e**,**f**, Typical waveforms of Rho (orange), F-actin (red), dilation rates (blue) and shear rates (green) in simulations (**e**) and the corresponding $\dot{S}$ measured from the autocorrelations (**f**). k_{RGA} defines the hydrolysis rate of Rho-GTP promoted by the expression of RGA-3/4. For each k_{RGA}, there are $n = 5$ independent simulations. Between $k_{RGA} = 0.40$ and 0.60 s^{-1}, $P = 2.8 \times 10^{-1}$ (Rho), 2.5×10^{-1} (F-actin), 7.8×10^{-6} (dilation) and 8.0×10^{-4} (shear). **g**–**i**, $\dot{S}$ produced by interacting Rho and F-actin ($\dot{S}_{RF}$) (**g**), F-actin and dilation rates ($\dot{S}_{Fd}$) (**h**), and Rho and dilation rates ($\dot{S}_{Rd}$) (**i**). The dashed lines in **g** indicate the linear fitting for data with [RGA-3/4] ≥ 166 ng μl^{-1} with 95% confidence bounds. The dashed lines in **h** and **i** indicate the linear fitting for data with [RGA-3/4] ≥ 333 ng μl^{-1} with 95% confidence bounds. For experiments, [RGA-3/4] = 0 ($n = 3$), 33 ($n = 5$), 66 ($n = 5$), 166 ($n = 16$), 333 ($n = 4$), 500 ($n = 4$) and 1,000 ng μl^{-1} ($n = 6$). For each k_{RGA} in simulations, $n = 5$. For **a**–**c**, data are presented as mean ± standard error. For **f**–**i**, data are presented as mean ± s.d. In **g**, $P = 5.4 \times 10^{-4}$, 5.2×10^{-1} and 6.5×10^{-1} between [RGA-3/4] = 0 and 66 ng μl^{-1}, [RGA-3/4] = 166 and 1,000 ng μl^{-1}, and [RGA-3/4] = 500 and 1,000 ng μl^{-1}, respectively. For the linear fitting of data within [RGA-3/4] = 166 and 1,000 ng μl^{-1}, $P = 4.9 \times 10^{-1}$. In **h**, $P = 2.8 \times 10^{-3}$ and 2.5×10^{-2} between [RGA-3/4] = 0 and 333 ng μl^{-1} and [RGA-3/4] = 333 and 1,000 ng μl^{-1}, respectively. For the linear fitting of data within [RGA-3/4] = 333 and 1,000 ng μl^{-1}, $P = 4.9 \times 10^{-2}$. In **i**, $P = 5.1 \times 10^{-3}$ and 2.2×10^{-2} between [RGA-3/4] = 0 and 333 ng μl^{-1} and [RGA-3/4] = 333 and 1,000 ng μl^{-1}, respectively. For the linear fitting of data within [RGA-3/4] = 333 and 1,000 ng μl^{-1}, $P = 4.4 \times 10^{-2}$. All the statistical comparisons between the two distributions were done with a two-sided t-test. We use the symbols *, **, *** and ***** for P values of <0.1, 0.01, 0.001 and 0.00001, respectively. ns, not significant. When fitting lines to data, we quote the P value as significance values to the rejections of null hypothesis.

https://doi.org/10.1038/s41567-024-02626-6

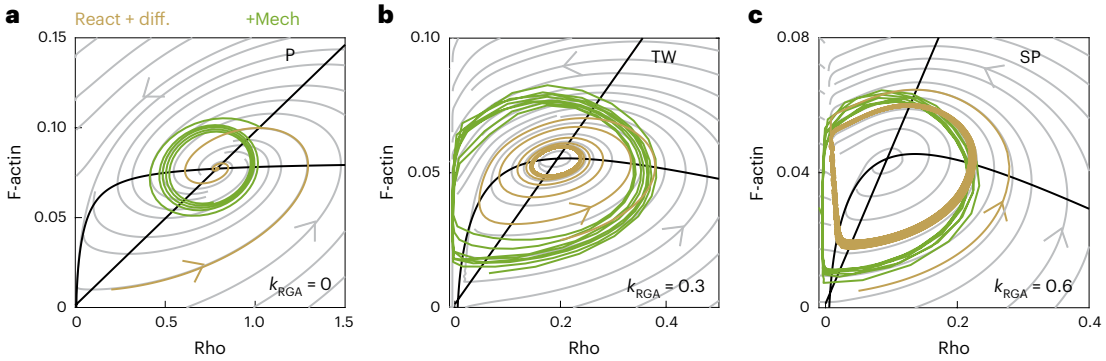

Fig. 3 | Mechanics get decoupled from chemical signalling in the highly activated cell cortex. Phase portrait analysis of different phenotypes in simulation: **a**, Pulses (P). **b**, Choppy travelling waves (TW). **c**, Spirals (SP). Black lines: Nullclines of Rho and F-actin dynamical equations. Grey trajectories: a simplified system with only reaction terms (Model). Orange trajectories: a simplified system with only reaction–diffusion terms (Model). Green trajectories: a complete system with coupled reaction–diffusion–advection terms (Model). k_{RGA} defines the hydrolysis rate of Rho-GTP promoted by the expression of RGA-3/4.

partitioned among each subsystem in a fixed proportion. To test this inference and gain a deeper understanding of the inherent cross-interactions amongst chemical and mechanical subsystems, we applied Onsager's form of $\dot{S}$ in the linear force–flux regime and Onsager reciprocal relations—a theory that describes interactions between different pairs of fluxes ($\mathcal{J}$) and forces ($\mathcal{F}$) in subsystems[48] (Fig. 4a).

We established the so-called Onsager matrix L (refs. 48,49) (Supplementary Note III). In Onsager's theory, when the system is near equilibrium, there is a linear force–flux relationship[50–52], based on which the Onsager matrix is constructed via $\mathcal{J}=L\cdot\mathcal{F}$ with equal off-diagonal coefficients, that is, $L_{AB}=L_{BA}$ ($A\neq B$), making L symmetric. In our case, we have three signals (R, F and $\mathbf{v}_c$); therefore, L is a 3 × 3 matrix. To quantify Onsager reciprocity between each pair of subsystems, we measured the absolute difference $|L_{12}-L_{21}|$, $|L_{23}-L_{32}|$ and $|L_{13}-L_{31}|$, which reflect the Rho/F-actin, F-actin/cortex motion and Rho/cortex motion interactions, respectively (Fig. 4a(iii) and Supplementary Fig. 14). Measurements from both experiments (Supplementary Figs. 10 and 14) and simulations (Fig. 4d and Supplementary Figs. 11 and 14) demonstrate that with modest [RGA-3/4] (modest k_{RGA}), $|L_{AB}-L_{BA}|\approx 0$, the pulsatile waves have a linear force–flux relationship (experiment, Supplementary Fig. 12; simulation, Supplementary Fig. 13) and the Onsager reciprocal relations are obeyed, as has been recently found for active systems in the linear-response regime[53–55]. Strikingly, however, with large RGA-3/4 (or large k_{RGA}), $|L_{AB}-L_{BA}|\gg 0$, the corresponding spiral waves have nonlinear force–flux relations (Supplementary Figs. 12 and 13) and broken Onsager reciprocal relations, as has been found with chiral active matter[56]. Interestingly, choppy travelling waves occur within but at the far end of the Onsager reciprocity (Supplementary Figs. 10d and 14) with linear force–flux relation (Supplementary Figs. 12 and 13).

To elucidate why energy partitioning among each subsystem is present in a fixed proportion at regimes with linear force–flux relation, we express $\dot{S}$ in Onsager's form[48] (Fig. 4a(i)). Here $\dot{S}_{\text{total}}=\sum_i(\mathcal{J}_i\cdot\mathcal{F}_i)=\sum_A\left(L_{AA}\mathcal{F}_A^2\right)+\sum_{(A\neq B)}\left(L_{AB}\mathcal{F}_B\mathcal{F}_A\right)$, which decomposes the total EPR into contributions from individual subsystems (with label A), and interactions between pairs of subsystems (with labels A and B). $\mathcal{J}_{\text{Rho}}$ and $\mathcal{J}_{\text{Act}}$ are the net reactional fluxes of Rho and F-actin, respectively. $\boldsymbol{\mathcal{J}}_{\text{M}}$ is the mass flow of the cortex. $\mathcal{F}_{\text{Rho}}$ and $\mathcal{F}_{\text{Act}}$ are the chemical affinities, and $\boldsymbol{\mathcal{F}}_{\text{C}}$ is the contractile force (Supplementary Note III). As evident from the simulation (Fig. 4b–d) by the ratio of the Onsager's rate of entropy ($\dot{S}$) produced by F-actin dynamics ($\mathcal{F}_{\text{Act}}\cdot\mathcal{J}_{\text{Act}}$) to that from Rho dynamics ($\mathcal{F}_{\text{Rho}}\cdot\mathcal{J}_{\text{Rho}}$) (Fig. 4b) and mechanical dynamics ($\boldsymbol{\mathcal{F}}_{\text{C}}\cdot\boldsymbol{\mathcal{J}}_{\text{M}}$) to F-actin dynamics (Fig. 4c), the broken reciprocal relations initiate from where the differential energy partitioning occurs, suggesting that energy is partitioned among chemical and mechanical subsystems in a fixed proportion for wave dynamics with Onsager reciprocity. Theoretical derivation under the constraint of linear force–flux assumption verifies this observation (Fig. 4b,c (dashed lines) and Supplementary Note III). Thus, we conclude that dynamic patterns in the cell cortex with Onsager reciprocity ([RGA-3/4] ≤ 166 ng μl^{-1} and $k_{RGA}<0.30\ \text{s}^{-1}$) cause the partitioning of energy between the chemical and mechanical subsystems in a fixed proportion. In particular, we found an EPR 'maximal' state at the far end of the Onsager-reciprocity regime, represented by choppy wave dynamics where (1) the EPR is maximized within the reciprocal regime with (2) strong coupling between the chemical and mechanical subsystems (as suggested by the coherence time measurement in Fig. 2b and phase portrait analysis in Fig. 3).

Competing timescales determine the repartition of energy

Next, we investigated the energy partitioning between the chemical and mechanical subsystems beyond the range of Onsager reciprocity by taking advantage of the computational model. Here we define two timescales: the chemical reaction rate $k_{\text{Chem}}=k_{RGA}$ and the characteristic mechanical relaxation rate $k_{\text{Mech}}=A_s/G\tau_{\text{ME}}$ (Supplementary Table 1).

In the computational model (Model; Supplementary Information), the chemical and mechanical subsystems are fully coupled by (1) actomyosin-induced contractile flow; (2) mechanical properties of the cell cortex affected by the F-actin concentration; (3) the advective transport of chemical species. Point (2) makes k_{Chem} a function of k_{Mech} (Fig. 5a,b, diamond symbols). To investigate the contribution of k_{Chem} and k_{Mech} to the energy partitioning independently, we decoupled k_{Chem} and k_{Mech} by making the shear modulus of the cortex (G) independent of the F-actin concentration. A phase diagram of decoupled k_{Chem} and k_{Mech} is shown in Fig. 5a, which captures all the wave phenotypes observed in the above sections. In Fig. 5b, we calculated the ratio of $\dot{S}_{\text{R}}$ to $\dot{S}_{\text{dil}}$, quantifying the proportion of chemical dissipation over mechanical dissipation. The results indicate that with fixed k_{Mech}, increasing k_{Chem} leads to more energy partitioned to the chemical subsystems, and vice versa. Moreover, it predicts a regime where the mechanical dynamics gain more energy, in contrast to our findings in the above sections. This implies that the chemical and mechanical timescales compete in a manner that determines the partitioning of energy beyond the range of Onsager reciprocity.

To experimentally verify this prediction, we performed experimental perturbations in which cofilin—an F-actin-severing protein—was overexpressed in vivo to increase the F-actin turnover (Supplementary Note I). As a result, the mechanical subsystem can operate on a faster timescale to keep up with chemical subsystems, reminiscent of an

https://doi.org/10.1038/s41567-024-02626-6

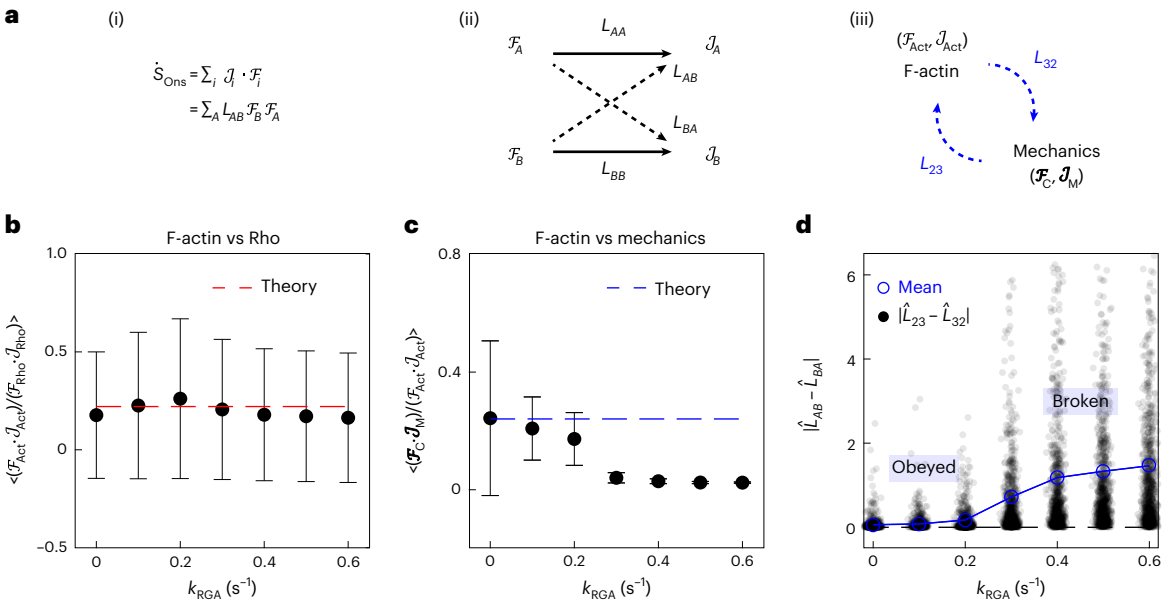

Fig. 4 | Onsager reciprocity implies energy partitioning among subsystems in a fixed proportion in simulation. a, Equation and coefficients in Onsager's theory: (i) expression of the total EPR $\dot{S}_{Ons}$, (ii) force–flux relationship and (iii) interactions between F-actin signalling and mechanical dynamics. **b**,**c**, Ratio of the Onsager's rate of entropy ($\dot{S}$) produced by F-actin dynamics ($\mathcal{F}_{Act} \cdot \mathcal{J}_{Act}$) to that from Rho dynamics ($\mathcal{F}_{Rho} \cdot \mathcal{J}_{Rho}$) (**b**) and mechanical dynamics ($\boldsymbol{\mathcal{F}}_C \cdot \boldsymbol{\mathcal{J}}_M$) to F-actin dynamics (**c**). Data are presented as mean ± s.d. **d**, Absolute difference of the off-diagonal Onsager's coefficients ($|L_{AB} - L_{BA}|$) manifesting the F-actin/mechanics interactions ($A = 2, B = 3$). Data are normalized by $L_{22} + L_{33}$. Open-coloured circles are the mean values connected by a solid line. The dashed lines are theoretical predictions. $|L_{23} - L_{32}| \approx 0$ with low k_{RGA} indicates an obeyed Onsager reciprocity, whereas $|L_{23} - L_{32}| \gg 0$ with large k_{RGA} indicates a broken Onsager reciprocity. $\mathcal{J}_A$ and $\mathcal{J}_B$ refer to the fluxes in subsystem A and B, respectively. $\mathcal{F}_A$ and $\mathcal{F}_B$ refer to the force in subsystems A and B, respectively. L_{AB} is the scaling factor that $\mathcal{F}_B$ has on $\mathcal{J}_A$, calculated from the Onsager matrix L that is constructed via $\mathcal{J} = L \cdot \mathcal{F}$. $\mathcal{J}_{Rho}$ and $\mathcal{J}_{Act}$ are the net reactional fluxes of Rho and F-actin, respectively. $\boldsymbol{\mathcal{J}}_M$ is the mass flow of the cortex. $\mathcal{F}_{Rho}$ and $\mathcal{F}_{Act}$ are the chemical affinities, and $\boldsymbol{\mathcal{F}}_C$ is the contractile force. k_{RGA} defines the hydrolysis rate of Rho-GTP promoted by the expression of RGA-3/4. L_{12} and L_{21}, L_{23} and L_{32}, and L_{13} and L_{31} reflect the phenomenological coefficients that are associated with Rho/F-actin, F-actin/cortex motion and Rho/cortex motion interactions, respectively. For each k_{RGA}, there are $n = 5$ independent simulations. For each simulation, a pair of forces ($\mathcal{F}_{Rho}$, $\mathcal{F}_{Act}$ and $\boldsymbol{\mathcal{F}}_C$) and fluxes ($\mathcal{J}_{Rho}$, $\mathcal{J}_{Act}$ and $\boldsymbol{\mathcal{J}}_M$), and their corresponding Onsager matrix L are calculated from 2,040 uniformly distributed grid points in space, with each grid containing 64 data points in time with equal time intervals. For demonstration, there are 1,000 randomly selected data points from datasets for each k_{RGA} in **d**.

increased k_{Mech} with roughly constant k_{Chem} in the model. Consequently, in cofilin experiments, the restoration of reciprocal relationship between F-actin dynamics and cortical motion (caused by their more coordinated interactions) is observed, compared with the control experiments (Fig. 5c). In Fig. 5d,e, we measured the $\dot{S}$ value produced by the chemical and mechanical subsystems, respectively. This indicated that there is less chemical dissipation but more mechanical dissipation in the wave dynamics in cofilin experiments compared with the control experiments, verifying our theoretical predictions.

Outlook

We manipulated energy consumption by the cell cortex via a graded expression of the Rho GAP RGA-3/4 and measured the EPR $\dot{S}$ during steady-state wave behaviours. This measure reflects the minimum energy required to sustain the observed processes, not the actual energy, which also includes dissipation that takes place below the optical resolution (due to ATP hydrolysis by actin and myosin and so on). By elevating GAP expression to drive the cell farther from equilibrium, we observed three sequential regimes: (1) pulsatile wave with Onsager reciprocity, characterized by energy partition in a fixed proportion; (2) choppy waves at the furthest extent of reciprocity also characterized by fixed energy partitioning; and (3) labyrinthine or spiral travelling waves with broken Onsager reciprocity and characterized by differential energy partitioning between two subsystems. In particular, the wave frequency (f) monotonically increases with increased driving. In contrast, however, only within the Onsager-reciprocity regime, displacing the system further from equilibrium increases $\dot{S}$ of both chemical and mechanical subsystems in the cell cortex and maintains strong coupling between them. This relationship between the overall energy consumption and cortical dynamics culminates at the far end of this regime, where $\dot{S}$ is maximized for both subsystems and is characterized by choppy waves with intermediate f. Intriguingly, this state of maximal $\dot{S}$ bears a striking resemblance, both qualitatively and quantitatively (with a frequency of approximately 0.01 s^{-1} (ref. 57)), to the cortical waves associated with cell division[31,39,57]. We speculate that this EPR maximal state within the reciprocity regime is particularly advantageous for cell division, as it ensures both high level of chemical/mechanical activities and chemical–mechanical coupling, potentially facilitating the robust functioning of cell division. A similar observation was also identified in crawling *Dictyostelium* cells[58], where actin oscillations associated with cell motility and chemotaxis were induced by a signalling stimulus. The most excitable state occurs neither with the most rapid nor the slowest stimulus, but at an intermediate state near the instability border where the signalling pathway and actin responses are well coordinated. In stark contrast, a departure from this state at high levels of GAP expression with broken Onsager reciprocity results in a differential energy partitioning among the now-uncoupled subsystems, where the mechanical activities struggle to keep pace with the excessively rapid chemical oscillations. It is essential to emphasize that such an uncoupled state can pose severe threats to the cell's viability and function[59]. For instance, impaired excitation–contraction coupling in the cardiac muscle, leading to a loss of synchronization between electrical and mechanical activities, is known to be a potentially life-threatening condition that culminates in sudden cardiac death[60].

Our results reveal fundamental principles in cellular energetics and non-equilibrium physics governing the intricate interplay between

https://doi.org/10.1038/s41567-024-02626-6

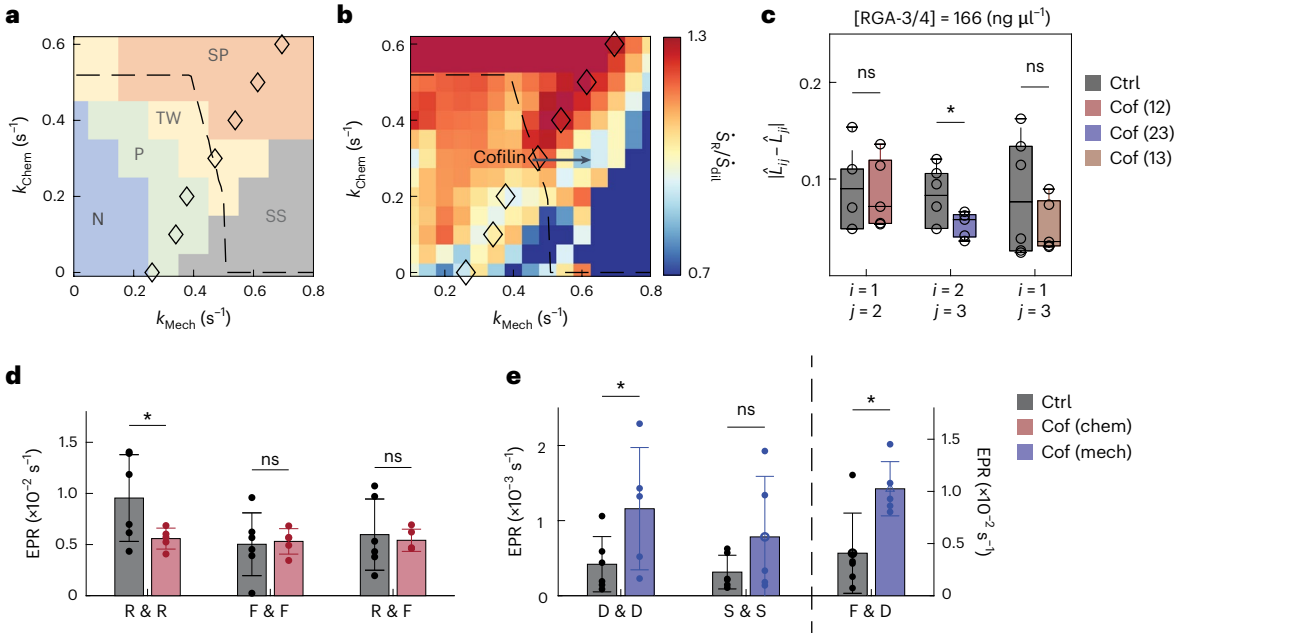

Fig. 5 | Competing internal timescales determine a repartition of energy. **a**, Phase plane (k_{Mech}, k_{Chem}) with different colour blocks classifying different wave phenotypes in simulation. N, noisy oscillations; P, pulses; TW, choppy or labyrinthine travelling waves; SS, self-reinforcing waves; SP, spirals. k_{Chem} and k_{Mech} are the chemical reaction rate and characteristic mechanical relaxation rate, respectively. **b**, Ratios of the EPR produced by Rho dynamics ($\dot{S}_R$) to the EPR produced by the dilation rates ($\dot{S}_{dil}$) on the (k_{Mech}, k_{Chem}) phase plane. The diamond symbols represent a fully coupled mechanochemical system with k_{Mech} as a function of k_{Chem}. The dashed line indicates the transition boundary to the spatiotemporal travelling waves. The arrow suggests a transition towards mechanics-dominant regime with overexpressed cofilin. **c**, Difference of the off-diagonal Onsager's coefficients ($|L_{ij} - L_{ji}|$) in cofilin experiments compared with control experiments manifesting the Rho/F-actin interactions (red; $i = 1$, $j = 2$, $P = 8.6 \times 10^{-1}$), F-actin/cortex motion interactions (blue; $i = 2, j = 3$, $P = 7.9 \times 10^{-2}$) and Rho/cortex motion interactions (orange; $i = 1, j = 3, P = 3.2 \times 10^{-1}$). Data are normalized by $L_{ii} + L_{jj}$. The grey bars mark the control experiments ($n = 6$), and coloured bars mark the cofilin experiments ($n = 5$). The box plot shows the interquartile range (IQR) between Q1 (25th percentile) and Q3 (75th percentile), with the centre line indicating the median. Whiskers are extended to Q3 + 1.5× IQR and Q1 − 1.5× IQR or to the maximum/minimum within this range. **d**, EPRs in cofilin experiments compared with the control experiments were measured from the autocorrelations of Rho signals ($\dot{S}_R$, R&R, $P = 7.3 \times 10^{-2}$), autocorrelations of F-actin signals ($\dot{S}_F$, F&F, $P = 8.5 \times 10^{-1}$) and cross-correlations of Rho/F-actin signals ($\dot{S}_{RF}$, R&F, $P = 7.4 \times 10^{-1}$). **e**, EPRs in cofilin experiments compared with control experiments were measured from the autocorrelations of dilation rates ($\dot{S}_{dil}$, D&D, $P = 7.6 \times 10^{-2}$), autocorrelations of shear rates ($\dot{S}_{shr}$, S&S, $P = 2.0 \times 10^{-1}$) and cross-correlations of F-actin/dilation rates ($\dot{S}_{Fd}$, F&D, $P = 1.4 \times 10^{-2}$). The grey bars mark the control experiments ($n = 6$), and the coloured bars mark the cofilin experiments ($n = 5$; red bars, chemical EPR; blue bars, mechanical EPR). For **d** and **e**, data are presented as mean ± s.d. All the statistical comparisons between two distributions were done with a two-sided *t*-test. We use the symbol * for *P* values of <0.1. ns, not significant.

energy partitioning and subsystem coupling in cellular dynamics. Furthermore, the underlying physics of cortical excitability clearly extends beyond embryonic cells[38], suggesting that our results and their implications will be relevant across diverse cell types.

Online content

Any methods, additional references, Nature Portfolio reporting summaries, source data, extended data, supplementary information, acknowledgements, peer review information; details of author contributions and competing interests; and statements of data and code availability are available at https://doi.org/10.1038/s41567-024-02626-6.

References

1. Niebel, B., Leupold, S. & Heinemann, M. An upper limit on Gibbs energy dissipation governs cellular metabolism. *Nat. Metab.* **1**, 125–132 (2019).
2. Yang, X. et al. Physical bioenergetics: energy fluxes, budgets, and constraints in cells. *Proc. Natl Acad. Sci. USA* **118**, e2026786118 (2021).
3. Ariga, T., Tomishige, M. & Mizuno, D. Nonequilibrium energetics of molecular motor kinesin. *Phys. Rev. Lett.* **121**, 218101 (2018).
4. Toyabe, S., Watanabe-Nakayama, T., Okamoto, T., Kudo, S. & Muneyuki, E. Thermodynamic efficiency and mechanochemical coupling of F_1-ATPase. *Proc. Natl Acad. Sci. USA* **108**, 17951–17956 (2011).
5. Lan, G., Sartori, P., Neumann, S., Sourjik, V. & Tu, Y. The energy–speed–accuracy trade-off in sensory adaptation. *Nat. Phys.* **8**, 422–428 (2012).
6. Tennessen, J. M., Baker, K. D., Lam, G., Evans, J. & Thummel, C. S. The *Drosophila* estrogen-related receptor directs a metabolic switch that supports developmental growth. *Cell Metab.* **13**, 139–148 (2011).
7. Jarzynski, C. Diverse phenomena, common themes. *Nat. Phys.* **11**, 105–107 (2015).
8. Ornes, S. How nonequilibrium thermodynamics speaks to the mystery of life. *Proc. Natl Acad. Sci. USA* **114**, 423–424 (2017).
9. Hong, S. et al. Sub-nanowatt microfluidic single-cell calorimetry. *Nat. Commun.* **11**, 2982 (2020).
10. Nagano, Y. & Ode, K. L. Temperature-independent energy expenditure in early development of the African clawed frog *Xenopus laevis*. *Phys. Biol.* **11**, 046008 (2014).
11. Auberson, L. C., Kanbier, T. & von Stockar, U. Monitoring synchronized oscillating yeast cultures by calorimetry. *J. Biotechnol.* **29**, 205–215 (1993).
12. Hur, S., Mittapally, R., Yadlapalli, S., Reddy, P. & Meyhofer, E. Sub-nanowatt resolution direct calorimetry for probing real-time metabolic activity of individual *C. elegans* worms. *Nat. Commun.* **11**, 2983 (2020).

13. Imamura, H. et al. Visualization of ATP levels inside single living cells with fluorescence resonance energy transfer-based genetically encoded indicators. *Proc. Natl Acad. Sci. USA* **106**, 15651–15656 (2009).
14. Yang, X., Ha, G. & Needleman, D. J. A coarse-grained NADH redox model enables inference of subcellular metabolic fluxes from fluorescence lifetime imaging. *eLife* **10**, e73808 (2021).
15. Wiechert, W. ^{13}C metabolic flux analysis. *Metab. Eng.* **3**, 195–206 (2001).
16. Park, J. S. et al. Mechanical regulation of glycolysis via cytoskeleton architecture. *Nature* **578**, 621–626 (2020).
17. Sakamoto, R. & Murrell, M. P. F-actin architecture determines the conversion of chemical energy into mechanical work. *Nat. Commun.* **15**, 3444 (2024).
18. Serra-Picamal, X. et al. Mechanical waves during tissue expansion. *Nat. Phys.* **8**, 628–634 (2012).
19. Banerjee, S., Utuje, K. J. & Marchetti, M. C. Propagating stress waves during epithelial expansion. *Phys. Rev. Lett.* **114**, 228101 (2015).
20. Alert, R. & Trepat, X. Physical models of collective cell migration. *Annu. Rev. Condens. Matter Phys.* **11**, 77–101 (2020).
21. Flemming, S., Font, F., Alonso, S. & Beta, C. How cortical waves drive fission of motile cells. *Proc. Natl Acad. Sci. USA* **117**, 6330–6338 (2020).
22. Boocock, D., Hino, N., Ruzickova, N., Hirashima, T. & Hannezo, E. Theory of mechanochemical patterning and optimal migration in cell monolayers. *Nat. Phys.* **17**, 267–274 (2021).
23. Munro, E., Nance, J. & Priess, J. R. Cortical flows powered by asymmetrical contraction transport PAR proteins to establish and maintain anterior-posterior polarity in the early *C. elegans* embryo. *Dev. Cell* **7**, 413–424 (2004).
24. Solon, J., Kaya-Copur, A., Colombelli, J. & Brunner, D. Pulsed forces timed by a ratchet-like mechanism drive directed tissue movement during dorsal closure. *Cell* **137**, 1331–1342 (2009).
25. Martin, A. C., Kaschube, M. & Wieschaus, E. F. Pulsed contractions of an actin–myosin network drive apical constriction. *Nature* **457**, 495–499 (2009).
26. Munjal, A., Philippe, J.-M., Munro, E. & Lecuit, T. A self-organized biomechanical network drives shape changes during tissue morphogenesis. *Nature* **524**, 351–355 (2015).
27. Bailles, A. et al. Genetic induction and mechanochemical propagation of a morphogenetic wave. *Nature* **572**, 467–473 (2019).
28. Wigbers, M. C. et al. A hierarchy of protein patterns robustly decodes cell shape information. *Nat. Phys.* **17**, 578–584 (2021).
29. Raskin, D. M. & De Boer, P. A. Rapid pole-to-pole oscillation of a protein required for directing division to the middle of *Escherichia coli*. *Proc. Natl Acad. Sci. USA* **96**, 4971–4976 (1999).
30. Sedzinski, J. et al. Polar actomyosin contractility destabilizes the position of the cytokinetic furrow. *Nature* **476**, 462–466 (2011).
31. Bement, W. M. et al. Activator–inhibitor coupling between Rho signalling and actin assembly makes the cell cortex an excitable medium. *Nat. Cell Biol.* **17**, 1471–1483 (2015).
32. Ramm, B. et al. A diffusiophoretic mechanism for ATP-driven transport without motor proteins. *Nat. Phys.* **17**, 850–858 (2021).
33. Murrell, M., Oakes, P. W., Lenz, M. & Gardel, M. L. Forcing cells into shape: the mechanics of actomyosin contractility. *Nat. Rev. Mol. Cell Biol.* **16**, 486–498 (2015).
34. Ajeti, V. et al. Wound healing coordinates actin architectures to regulate mechanical work. *Nat. Phys.* **15**, 696–705 (2019).
35. Banerjee, S., Gardel, M. L. & Schwarz, U. S. The actin cytoskeleton as an active adaptive material. *Annu. Rev. Condens. Matter Phys.* **11**, 421–439 (2020).
36. Wu, M. & Liu, J. Mechanobiology in cortical waves and oscillations. *Curr. Opin. Cell Biol.* **68**, 45–54 (2021).
37. Yan, V. T., Narayanan, A., Wiegand, T., Jülicher, F. & Grill, S. W. A condensate dynamic instability orchestrates actomyosin cortex activation. *Nature* **609**, 597–604 (2022).
38. Bement, W. M., Goryachev, A. B., Miller, A. L. & von Dassow, G. Patterning of the cell cortex by Rho GTPases. *Nat. Rev. Mol. Cell Biol.* **25**, 290–308 (2024).
39. Michaud, A. et al. A versatile cortical pattern-forming circuit based on Rho, F-actin, Ect2, and RGA-3/4. *J. Cell Biol.* **221**, e202203017 (2022).
40. Benink, H. A., Mandato, C. A. & Bement, W. M. Analysis of cortical flow models in vivo. *Mol. Biol. Cell* **11**, 2553–2563 (2000).
41. Markovich, T., Fodor, É., Tjhung, E. & Cates, M. E. Thermodynamics of active field theories: energetic cost of coupling to reservoirs. *Phys. Rev.* **11**, 021057 (2021).
42. Seara, D. S., Machta, B. B. & Murrell, M. P. Irreversibility in dynamical phases and transitions. *Nat. Commun.* **12**, 392 (2021).
43. Zhang, D., Cao, Y., Ouyang, Q. & Tu, Y. The energy cost and optimal design for synchronization of coupled molecular oscillators. *Nat. Phys.* **16**, 95–100 (2020).
44. Lynn, C. W., Holmes, C. M., Bialek, W. & Schwab, D. J. Decomposing the local arrow of time in interacting systems. *Phys. Rev. Lett.* **129**, 118101 (2022).
45. Cao, Y., Wang, H., Ouyang, Q. & Tu, Y. The free-energy cost of accurate biochemical oscillations. *Nat. Phys.* **11**, 772–778 (2015).
46. Oberreiter, L., Seifert, U. & Barato, A. C. Universal minimal cost of coherent biochemical oscillations. *Phys. Rev. E* **106**, 014106 (2022).
47. Marsland, R., Cui, W. & Horowitz, J. M. The thermodynamic uncertainty relation in biochemical oscillations. *J. R. Soc. Interface* **16**, 20190098 (2019).
48. Onsager, L. Reciprocal relations in irreversible processes. I. *Phys. Rev.* **37**, 405 (1931).
49. Ohga, N., Ito, S. & Kolchinsky, A. Thermodynamic bound on the asymmetry of cross-correlations. *Phys. Rev. Lett.* **131**, 077101 (2023).
50. Gingrich, T. R., Rotskoff, G. M. & Horowitz, J. M. Inferring dissipation from current fluctuations. *J. Phys. A: Math. Theor.* **50**, 184004 (2017).
51. Qiu, Y., Nguyen, M., Hocky, G. M., Dinner, A. R. & Vaikuntanathan, S. A strong nonequilibrium bound for sorting of cross-linkers on growing biopolymers. *Proc. Natl Acad. Sci. USA* **118**, e2102881118 (2021).
52. Chun, H.-M., Gao, Q. & Horowitz, J. M. Nonequilibrium Green-Kubo relations for hydrodynamic transport from an equilibrium-like fluctuation-response equality. *Phys. Rev. Research* **3**, 043172 (2021).
53. Luo, R., Benenti, G., Casati, G. & Wang, J. Onsager reciprocal relations with broken time-reversal symmetry. *Phys. Rev. Res.* **2**, 022009 (2020).
54. Wang, X., Dobnikar, J. & Frenkel, D. Numerical test of the Onsager relations in a driven system. *Phys. Rev. Lett.* **129**, 238002 (2022).
55. De Corato, M. & Pagonabarraga, I. Onsager reciprocal relations and chemo-mechanical coupling for chemically active colloids. *J. Chem. Phys.* **157**, 084901 (2022).
56. Banerjee, D., Souslov, A., Abanov, A. G. & Vitelli, V. Odd viscosity in chiral active fluids. *Nat. Commun.* **8**, 1573 (2017).
57. Swider, Z. T. et al. Cell cycle and developmental control of cortical excitability in *Xenopus laevis*. *Mol. Biol. Cell* **33**, ar73 (2022).
58. Westendorf, C. et al. Actin cytoskeleton of chemotactic amoebae operates close to the onset of oscillations. *Proc. Natl Acad. Sci. USA* **110**, 3853–3858 (2013).

59. Cunnane, S. C. et al. Brain energy rescue: an emerging therapeutic concept for neurodegenerative disorders of ageing. *Nat. Rev. Drug Discov.* **19**, 609–633 (2020).
60. Kistamas, K. et al. Calcium handling defects and cardiac arrhythmia syndromes. *Front. Pharmacol.* **11**, 72 (2020).

Methods

The acquisition of *Xenopus* oocytes was performed in accordance with relevant animal ethical guidelines and regulations under animal care protocol G005386-R01, administered by the University of Wisconsin–Madison Institutional Animal Care and Use Committee. Methods and any associated references are available in the Supplementary Information. Sample sizes were chosen based on previous studies of cortical wave dynamics[39]. The oocytes were randomly assigned to injection groups after isolation. Data collection and analysis were performed automatically by codes, without prior knowledge of the experimental conditions. Data were collected using PrairieView software. Dead cells or cells with invisible pigment granules were excluded. Data distribution was assumed to be normal, but this was not formally tested.

Reporting summary

Further information on research design is available in the Nature Portfolio Reporting Summary linked to this article.

Data availability

Data supporting the findings of this study are available from the corresponding authors upon reasonable request. Source data are provided with this paper.

Code availability

Custom codes that were used for the data analysis in this manuscript are available via GitHub at http://github.com/shengchen-yale/mech-chem-wave.

Acknowledgements

We acknowledge funding through ARO MURI W911NF-14-1-0403 (to M.P.M.), National Institutes of Health RO1 GM126256 (to M.P.M.), NIH U54 CA209992 (to M.P.M.), Human Frontier Science Program (HFSP) grant no. RGY0073/2018 (to M.P.M.), National Institutes of Health grant RO1GM052932 (to W.M.B.) and NSF grant 2132606 (to W.M.B.). Any opinion, findings and conclusions or recommendations expressed in this material are those of the authors and do not necessarily reflect the views of the NIH, NSF, ARO or HFSP. We acknowledge helpful discussions with B. Machta, H. Levine, S. Amiri and J. Ke.

Author contributions

M.P.M. and W.M.B. designed and conceived the project. W.M.B. designed and conceived the experimental work. M.P.M., S.C. and D.S.S. designed and conceived the analytical, computational and theoretical work. W.M.B., A.M. and S.K. performed the experiments. S.C. and D.S.S. analysed the experimental data. S.C. implemented the model and performed and analysed the simulations. S.C. conducted the theoretical analysis. D.S.S. performed the theoretical analysis of the Stuart–Landau equation. S.C., D.S.S., W.M.B. and M.P.M. wrote the manuscript.

Competing interests

The authors declare no competing interests.

Additional information

Supplementary information The online version contains supplementary material available at https://doi.org/10.1038/s41567-024-02626-6.

Correspondence and requests for materials should be addressed to William M. Bement or Michael P. Murrell.

Peer review information *Nature Physics* thanks the anonymous reviewers for their contribution to the peer review of this work.

nature portfolio

Corresponding author(s): William M. Bement, Michael P. Murrell

Last updated by author(s): June 26, 2024

Reporting Summary

Nature Portfolio wishes to improve the reproducibility of the work that we publish. This form provides structure for consistency and transparency in reporting. For further information on Nature Portfolio policies, see our Editorial Policies and the Editorial Policy Checklist.

Statistics

For all statistical analyses, confirm that the following items are present in the figure legend, table legend, main text, or Methods section.

n/a	Confirmed	
☐	☒	The exact sample size (*n*) for each experimental group/condition, given as a discrete number and unit of measurement
☐	☒	A statement on whether measurements were taken from distinct samples or whether the same sample was measured repeatedly
☐	☒	The statistical test(s) used AND whether they are one- or two-sided *Only common tests should be described solely by name; describe more complex techniques in the Methods section.*
☒	☐	A description of all covariates tested
☐	☒	A description of any assumptions or corrections, such as tests of normality and adjustment for multiple comparisons
☐	☒	A full description of the statistical parameters including central tendency (e.g. means) or other basic estimates (e.g. regression coefficient) AND variation (e.g. standard deviation) or associated estimates of uncertainty (e.g. confidence intervals)
☐	☒	For null hypothesis testing, the test statistic (e.g. *F*, *t*, *r*) with confidence intervals, effect sizes, degrees of freedom and *P* value noted *Give P values as exact values whenever suitable.*
☒	☐	For Bayesian analysis, information on the choice of priors and Markov chain Monte Carlo settings
☒	☐	For hierarchical and complex designs, identification of the appropriate level for tests and full reporting of outcomes
☒	☐	Estimates of effect sizes (e.g. Cohen's *d*, Pearson's *r*), indicating how they were calculated

Our web collection on statistics for biologists contains articles on many of the points above.

Software and code

Policy information about availability of computer code

Data collection	Prairie View software
Data analysis	Custom written MATLAB (R) version 2022a script was used for data analysis. ImageJ version 1.53k was used for basic image processing COMSOL Multiphysics version 5.2a-classkit was used for computational simulation Custom codes that were used for data analysis within this manuscript can be found at http://github.com/shengchen-yale/mech-chem-wave.

For manuscripts utilizing custom algorithms or software that are central to the research but not yet described in published literature, software must be made available to editors and reviewers. We strongly encourage code deposition in a community repository (e.g. GitHub). See the Nature Portfolio guidelines for submitting code & software for further information.

Data

Policy information about availability of data

All manuscripts must include a data availability statement. This statement should provide the following information, where applicable:

- Accession codes, unique identifiers, or web links for publicly available datasets
- A description of any restrictions on data availability
- For clinical datasets or third party data, please ensure that the statement adheres to our policy

Data supporting the finding of this manuscript are available from the corresponding author upon reasonable request. The data generated in this study are provided in the Source Data file. We used the open source ImageJ/Fiji available at https://imagej.net/ij/index.html

Human research participants

Policy information about studies involving human research participants and Sex and Gender in Research.

Reporting on sex and gender	N/A
Population characteristics	N/A
Recruitment	N/A
Ethics oversight	N/A

Note that full information on the approval of the study protocol must also be provided in the manuscript.

Field-specific reporting

Please select the one below that is the best fit for your research. If you are not sure, read the appropriate sections before making your selection.

☒ Life sciences ☐ Behavioural & social sciences ☐ Ecological, evolutionary & environmental sciences

For a reference copy of the document with all sections, see nature.com/documents/nr-reporting-summary-flat.pdf

Life sciences study design

All studies must disclose on these points even when the disclosure is negative.

Sample size	Sample sizes were chosen based on previous studies of cortical wave dynamics (Michaud et al., 2022. pubmed id: 35708547)
Data exclusions	Dead cells or cells with invisible pigment granules were excluded.
Replication	Experiments were replicated on multiple cells from multiple experiments; the sample sizes are indicated in the figures or figure legends.
Randomization	The oocytes were randomly assigned to injection groups after isolation.
Blinding	Data collection and analysis were performed automatically by codes, without prior knowledge of the experimental conditions.

Reporting for specific materials, systems and methods

We require information from authors about some types of materials, experimental systems and methods used in many studies. Here, indicate whether each material, system or method listed is relevant to your study. If you are not sure if a list item applies to your research, read the appropriate section before selecting a response.

Materials & experimental systems

n/a	Involved in the study
☒	☐ Antibodies
☒	☐ Eukaryotic cell lines
☒	☐ Palaeontology and archaeology
☐	☒ Animals and other organisms
☒	☐ Clinical data
☒	☐ Dual use research of concern

Methods

n/a	Involved in the study
☒	☐ ChIP-seq
☒	☐ Flow cytometry
☒	☐ MRI-based neuroimaging

Animals and other research organisms

Policy information about studies involving animals; ARRIVE guidelines recommended for reporting animal research, and Sex and Gender in Research

Laboratory animals	Xenopus laevis
Wild animals	N/A
Reporting on sex	N/A
Field-collected samples	N/A
Ethics oversight	The acquisition of Xenopus oocytes was performed in accordance with relevant animal ethical guidelines and regulations under animal care protocol G005386-R01, administered by the University of Wisconsin-Madison Institutional Animal Care and Use Committee.

Note that full information on the approval of the study protocol must also be provided in the manuscript.